Letter

Timekeeping precision enhancements at constant power

K. J. H. Peters [1], B. Braeckeveldt [2], B. Maes [2], and S. R. K. Rodriguez [1,*]

[1] *Center for Nanophotonics, AMOLF, Science Park 104, 1098 XG Amsterdam, The Netherlands*

[2] *Micro- and Nanophotonic Materials Group, Research Institute for Materials Science and Engineering, University of Mons, 20 Place du Parc, Mons B-7000, Belgium*

(Received 13 August 2025; accepted 25 November 2025; published 12 January 2026)

We study the precision of a noisy clock comprising laser-driven coupled optical cavities sustaining limit cycles. We quantify the timekeeping precision of this system via the standard deviation of the limit-cycle period and demonstrate how it changes when varying the cavity length. We find timekeeping precision enhancements at constant power and regardless of the operation frequency. Through a phase space analysis of the limit-cycle fluctuations, we reveal how the proximity of different bifurcations determines the timekeeping precision of our system regardless of the input power and oscillation frequency. We expect our results to assist in the design of clocks that must operate in the presence of strong fluctuations, such as small clocks influenced by thermal noise. While fluctuations inevitably limit the maximum precision that can be attained, our results elucidate how that limited precision can be substantially enhanced while maintaining the energy efficiency and operation frequency of the clock.

DOI: 10.1103/pym4-3csj

Keeping track of time is essential for information processing. Consider, for example, the internal clocks of mammals and digital computers. Without these clocks, the synchronization and ordering of events necessary for life and computation cannot emerge. A clock's precision is limited by thermodynamics [1–9]. There exists a minimum energy required to maintain a clock's precision given a noise strength [1,2]. However, most clocks operate above this ultimate limit, where the relation between energy and precision can be subtle.

Nonlinear systems supporting stable limit cycles—attracting isolated closed orbits in phase space [10]—are ideal models of clocks. Their self-sustained oscillations can provide a time reference [11]. While not essential for timekeeping, limit-cycle oscillators are superior clocks in noisy environments [4]. When the oscillator is perturbed away from the attracting orbit, the limit-cycle oscillations persist provided that the fluctuation does not launch the system into another attractor. These limit-cycle oscillators have inspired many advances in physics and adjacent fields, including recent theories about their origin [12]. Limit cycles can emerge in circadian [4,13,14], neural [15–17], optical [18–22], mechanical [23,24], optomechanical [25–28], and electromechanical [29] systems, to name a few examples. In the past decade, interest in limit cycles surged with the advent of time crystals [30–40]: time-periodic states emerging through spontaneous breaking of time-translation symmetry. Such a symmetry breaking also occurs at the onset of a limit cycle, where its phase is randomly selected [37]. In the context of both time crystals and clocks, understanding how fluctuations affect self-sustained oscillations is one of the main goals [41]. This understanding is necessary to create precise and robust clocks, especially when fluctuations are prominent and energy is limited.

Here, we explore the nontrivial relation between input power and timekeeping precision in the regime of strong fluctuations. We demonstrate precision enhancements at constant input power. We present experiments and theory for a laser-driven coupled-cavity system sustaining stable limit cycles, thereby functioning as a clock. The cavity length is tunable. This enables us to scan the laser-cavity frequency detuning, and makes our system strongly susceptible to fluctuations. Contrary to the intuition that a clock's energy consumption and frequency determine its precision, we observe substantial precision enhancements at constant power and with minor frequency changes. We achieve this by controlling the proximity of the limit cycle to different bifurcations via the tunable cavity length. As those bifurcations influence the limit-cycle fluctuations, the timekeeping precision is thereby modified. Our experimental results are supported by numerical simulations, enabling us to analyze fluctuations in phase space. We conclude by offering perspectives for our results.

Figure 1(a) illustrates our experimental system: Two coupled side-by-side microcavities (details in Appendix A) filled with olive oil and driven by a continuous wave laser. The oil partly absorbs the laser light, warms up, expands, and its refractive index thereby changes. This makes the cavity optical response nonlinear [42,43]. Taking this into account, the light fields $\alpha_{1,2}$ in our oil-filled coupled cavities obey the following equations of motion in a frame rotating at the laser

*Contact author: s.rodriguez@amolf.nl

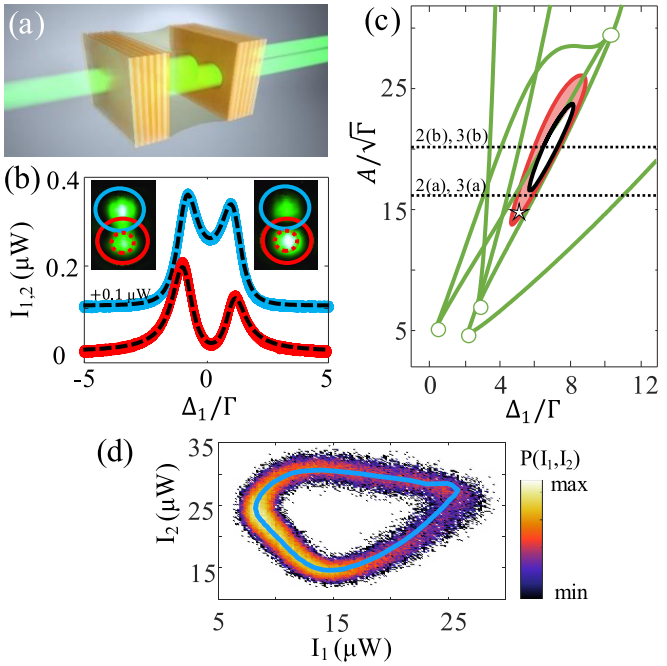

FIG. 1. (a) Two oil-filled coupled cavities. (b) Intensities transmitted by the laser-driven (I_1, solid red) and undriven (I_2, solid blue, displaced for clarity) cavities as a function of the laser-cavity detuning Δ_1/Γ, in the linear regime. Black dashed curves are steady-state solutions of Eq. (1). Insets: transmission images of the bonding (left) and antibonding (right) modes. Solid red and blue circles enclose the driven and undriven cavity, respectively. Dashed red circles indicate the location of the driving laser. (c) Curves of saddle-node (green), Hopf (red), and homoclinic (black) bifurcations, predicted by Eq. (1). Cusp bifurcations are shown as open green circles. Limit cycles are expected in the red shaded region. (d) Experimentally obtained joint probability distribution of $I_{1,2}$ at the driving conditions indicated by the star in panel (c). The blue curve is the experimentally obtained mean limit cycle.

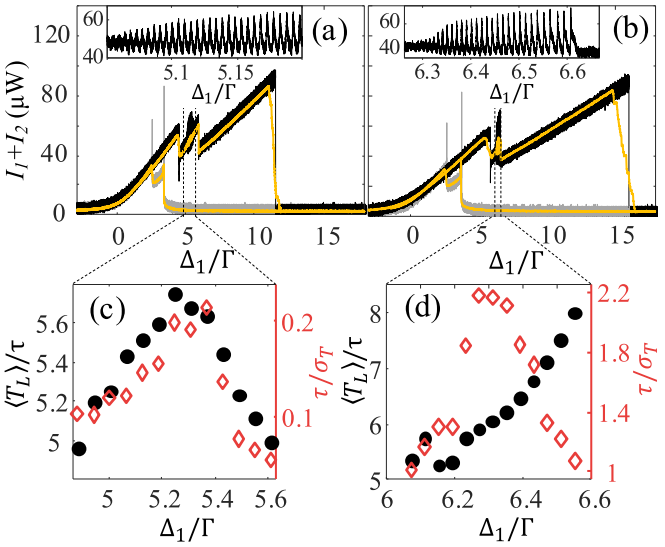

FIG. 2. Panels (a) and (b) show the intensity transmitted by both cavities when scanning the detuning forward (black) and back (gray) with a fixed laser power of 7.9 and 9.8 mW, respectively. Black curves are a single shot, and yellow curves are the average of 40 scans. Insets: Close-up into the oscillations. (c), (d) Average oscillation period (black dots) and precision (red diamonds) as a function of Δ_1/Γ for driving conditions corresponding to panels (a) and (b).

frequency ω:

$$i\dot{\alpha}_j(t) = \Big[-\Delta_j - i\Big(\frac{\Gamma}{2} + \beta|\alpha_j(t)|^2\Big) + U\int_0^t ds\, K(t-s)|\alpha_j(s)|^2\Big]\alpha_j(t) + i\sqrt{\kappa_L}[1-(-1)^j\rho]A - J\alpha_{3-j}(t) + D\xi_j(t). \quad (1)$$

$\Delta_j = \omega - \omega_j$ is the frequency detuning between the laser and the jth cavity resonance ω_j. $\Gamma = \gamma + \kappa_L + \kappa_R$ is the total loss rate of each cavity, including absorption γ and input-output losses through the left (right) mirror κ_L (κ_R). β is the strength of nonlinear losses, necessary to reproduce our experimental observations (see the Supplemental Material [44]). U is the thermo-optical nonlinearity strength, and $K(t) = \exp(-t/\tau)/\tau$ is a memory kernel characterizing the oil's thermal relaxation time. τ is the thermal relaxation time as well as the memory time of the system. Following the approach in Ref. [43] and summarized in Appendix B, we estimate $\tau = 1.2$ μs for our system. γ, β, U, and τ are equal for both cavities since they are both filled with the same oil. Γ could in principle be different for each cavity, since small asymmetries could imbalance $\kappa_{L,R}$ for the two cavities. However, we observe no signatures of this effect in our experiments. A is the laser amplitude, with $\rho \in [-1, 1]$ the driving imbalance between cavities. J is the intercavity coupling rate. $D\xi_j(t) = D[\xi_j^R(t) + i\xi_j^I(t)]/\sqrt{2}$ are Gaussian white noises with zero mean, correlations $\langle \xi_i(t)\xi_j(t')\rangle = \delta_{ij}\delta(t-t')$, and variance D^2, accounting for amplitude and phase noise in the driving laser. The same stochastic terms account for fluctuations in the intracavity field, assuming all noise sources are white, Gaussian, and additive. Details about our model and its numerical implementation are reported in Appendix C.

Figure 1(b) shows the experimental intensity transmitted by each cavity when driving only the lower cavity at a low laser power, ensuring linear response. We also plot the steady-state solutions of Eq. (1), with parameter values chosen to fit our experimental data. Fitting the model to our data in this way, we obtained the values of ρ, J, and the intercavity detuning $\delta = \Delta_2 - \Delta_1$ corresponding to our experiments. Figure 1(c) shows the two-parameter bifurcation diagram for our system, obtained via numerical continuation using the Matlab toolbox MatCont [45]. In the Supplemental Material [44], we present experimental signatures of all predicted bifurcations. Limit cycles are expected in the shaded red region of Fig. 1(c). Measuring the transmitted intensities $I_{1,2}$ in that region, at the location of the star in Fig. 1(c), we indeed observe a limit cycle as shown in Fig. 1(d). The mean evolution (blue curve) forms an isolated closed orbit in the $I_{1,2}$ plane, and the joint probability distribution $P(I_1, I_2)$ (encoded in color) forms a ring around it. The width of that ring is determined by the noise variance.

Figures 2(a) and 2(b) show the total transmitted intensity $I_1 + I_2$, while scanning the cavity length in the nonlinear

regime, at 7.9 and 9.8 mW, respectively. These two laser powers are indicated by the dashed lines in Fig. 1(c). Black and gray curves are single scans whereby the detuning increases and decreases, respectively. Yellow curves are the average of ∼40 scans. For both laser powers, we observe a large hysteresis and several jumps due to saddle-node bifurcations corresponding to the green curves in Fig. 1(c). We also observe limit cycles within certain detuning ranges [$4.95 \lesssim \Delta_1/\Gamma \lesssim 5.6$ in Fig. 2(a) and $6.1 \lesssim \Delta_1/\Gamma \lesssim 6.55$ in Fig. 2(b)], as shown, for example, in the insets of Figs. 2(a) and 2(b). In the Supplemental Material [44], we show that, for both laser powers, the oscillation amplitude initially increases as the detuning increases. Upon approaching a Hopf bifurcation in Fig. 2(a), the oscillations gradually decrease in amplitude. In contrast, upon approaching a homoclinic bifurcation in Fig. 2(b), the oscillations terminate abruptly and their period diverges. At that homoclinic bifurcation [black curve in Fig. 1(c)], the limit cycle collides with a saddle (unstable fixed point) and disappears.

We now focus on the detuning ranges supporting limit cycles, enclosed by dotted lines in Figs. 2(a) and 2(b). Figures 2(c) and 2(d) show the average limit-cycle period $\langle T_L \rangle$ and its inverse standard deviation σ_T^{-1}, both referenced to τ. We use τ/σ_T to quantify the timekeeping precision: The smaller the variance of the limit-cycle period, the greater the precision of a timekeeping device. The limit cycles in Fig. 2(c) are bound by Hopf bifurcations on both sides. Within this detuning range, τ/σ_T changes by a factor of 4, while $\langle T_L \rangle/\tau$ changes by merely ∼10%. Already this result demonstrates substantial timekeeping precision enhancements at constant power and minor frequency changes. Interestingly, the precision is maximized when the operation frequency is minimized. This opposes the widely held expectation that a clock's precision is proportional to its frequency. Figure 2(d), corresponding to a larger laser power, also shows substantial timekeeping precision enhancements at an intermediate detuning. τ/σ_T follows a trend similar to that in Fig. 2(c), reaching a maximum at an intermediate detuning. However, unlike in Fig. 2(c), $\langle T_L \rangle/\tau$ increases steadily with detuning. According to theory, the limit-cycle period should diverge upon approaching the homoclinic bifurcation on the right. Figure 2(d) indeed shows a progressive growth of $\langle T_L \rangle/\tau$, in qualitative agreement with theory. However, nanoscale vibrations of our experimental cavity setup prevent us from further approaching the homoclinic bifurcation and hence the divergence of the limit-cycle period. Overall, Figs. 2(c) and 2(d), combined, demonstrate the generality of the phenomenon we study: timekeeping precision variations at constant power.

Next, we elucidate the physics of our system using our model. To this end, we first validated our model (see the Supplemental Material [44]) by reproducing our experimental observations across a range of detunings and laser powers. Figures 3(a) and 3(b) present an analysis similar to that in Figs. 2(c) and 2(d), but for numerical data. Here, the laser amplitude A is referenced to the critical value for bistability, A_c (see Appendix C). We calculated $\langle T_L \rangle/\tau$ via numerical continuation and τ/σ_T via stochastic simulations. For both laser powers, we reproduce our three main observations: (1) τ/σ_T is maximized at an intermediate detuning; (2) $\langle T_L \rangle/\tau$ slightly decreases upon approaching a Hopf bifurcation [Fig. 3(a)], and

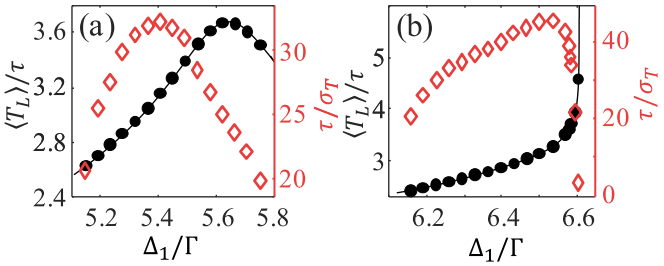

FIG. 3. (a) Average oscillation period (black dots) and precision (red diamonds) vs Δ_1/Γ for a constant laser amplitude $A = 3.9A_c$. Black curves are obtained via numerical continuation of the limit cycle. (b) Same as panel (a) but for $A = 4.9A_c$.

increases more substantially upon approaching a homoclinic bifurcation [Fig. 3(b)]; and (3) τ/σ_T does not, in general, correlate with $\langle T_L \rangle/\tau$. We also notice three discrepancies between experiments and simulations: (1) The values of τ/σ_T are different; (2) peaks in $\langle T_L \rangle/\tau$ and τ/σ_T are slightly shifted in detuning; and (3) τ/σ_T drops substantially upon approaching the homoclinic bifurcation in Fig. 3(b), where the limit-cycle period diverges. We believe that discrepancies (1) and (2) can be attributed to our use of a much shorter thermal relaxation time in simulations ($\Gamma\tau = 5000$) compared to experiments ($\Gamma\tau \sim 10^5$). The shorter relaxation time was necessary due to computer memory limitations, as explained in Appendix C. Discrepancy (3), we believe, is due to the intrinsic experimental difficulty in approaching a homoclinic bifurcation without crossing it. The three discrepancies are nonetheless inconsequential to our study, focused on understanding qualitative changes in timekeeping precision at constant input power. Those changes are similarly evident in both experiments and simulations.

We now explain our observations, which are related to the enhancement of fluctuations near a bifurcation [46–48]. To this end, we analyze intensity fluctuations in the directions normal and tangent to the deterministic limit cycle in the plane of transmitted intensities, as illustrated in Fig. 4. We performed this analysis on numerical data because our experimental setup does not provide a sufficiently smooth limit cycle resembling the deterministic one, even after substantial averaging. The black curve in Fig. 4 is the deterministic limit cycle. The gray curve is a typical stochastic limit cycle, with its last two points labeled $\mathbf{p}_{i,j}$. We set up a moving reference frame with unit vectors $\hat{\mathbf{T}}$ and $\hat{\mathbf{N}}$ in the directions tangent and normal to the deterministic limit cycle, respectively. Fluctuations normal to the deterministic limit cycle are defined as the distance n from a point $\mathbf{p}_j$ on the stochastic trajectory to the deterministic limit cycle. n therefore corresponds to the projection of $\mathbf{p}_j$ onto $\hat{\mathbf{N}}$ (indicated for the last point on the stochastic trajectory in Fig. 4).

Based on 8000 stochastic limit cycles, we obtained a joint probability distribution $P(N_1, N_2)$. $N_1 = |\alpha_1|^2$ and $N_2 = |\alpha_2|^2$ correspond to the intensities I_1 and I_2, respectively. We can then define an effective potential $V_{\text{eff}} = -\ln[P(N_1, N_2)]$ for the limit cycle, shown as a colored surface in Fig. 4. The local curvature in the normal direction is computed as $k = \frac{d^2 V_{\text{eff}}}{dn^2}|_{n=0}$. Intuitively, k can be interpreted as the spring

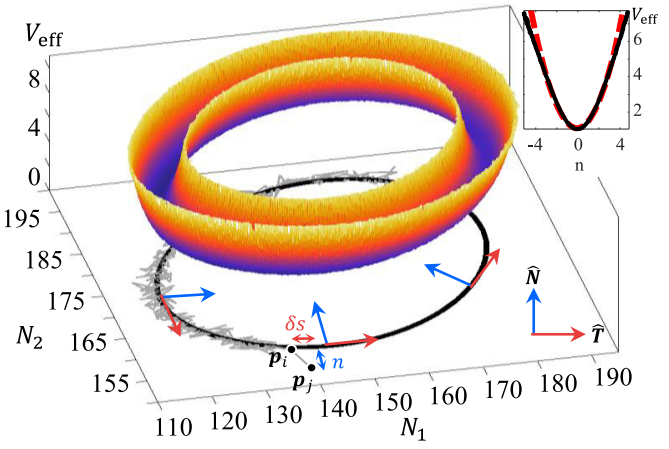

FIG. 4. Colored surface: effective potential V_{eff} for the limit cycle. Black curve: deterministic limit cycle. Gray curve: part of one stochastic limit cycle. Red and blue arrows: tangent and normal unit vectors, $\hat{\mathbf{T}}$ and $\hat{\mathbf{N}}$. Black dots labeled $\mathbf{p}_{i,j}$ indicate the last two points of the trajectory, illustrating the definitions of normal deviation n and arclength change δs. Inset: V_{eff} vs n in black. Red dashed curve is a parabolic fit.

constant of the restoring force in the direction normal to the mean limit cycle. Thus, the stochastic limit cycle is more strongly confined when k is larger. Assuming a fixed noise variance, deviations in the normal direction are less prominent under strong confinement of the limit cycle.

Figures 5(a) and 5(b) show the curvature averaged over the full cycle, $\langle k \rangle$, as a function of Δ_1/Γ for the two laser powers under consideration. In Fig. 5(b), we observe how $\langle k \rangle$ closely follows the trend of τ/σ_T in Fig. 3(b). However, $\langle k \rangle$ in Fig. 5(a) shows qualitatively different behavior from τ/σ_T in Fig. 3(a). Notice how $\langle k \rangle$ increases with Δ_1/Γ.

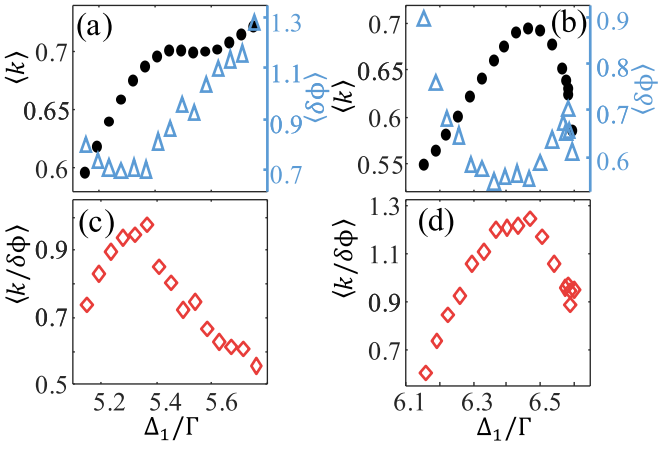

FIG. 5. (a), (b) Mean curvature $\langle k \rangle$ (black circles) and phase shift $\langle \delta\phi \rangle$ (blue triangles) vs Δ_1/Γ at constant power. All model parameters for panels (a) and (b) are as in Figs. 3(c) and 3(d), respectively. The ratio $\langle k/\delta\phi \rangle$, which qualitatively reproduced the experimentally observed timekeeping precision, is plotted in panels (c) and (d) for the driving conditions in panels (a) and (b), respectively.

This trend reproduces the initial rise in τ/σ_T in Fig. 3(a), but does not explain the decrease at large detuning. Clearly, $\langle k \rangle$ cannot explain the dependence of the timekeeping precision on detuning for this laser power. A more general explanation, capturing the behavior at both laser powers, is needed.

While $\langle k \rangle$ influences fluctuations normal to the deterministic limit cycle, fluctuations in the tangent direction can lead to phase diffusion. Stochastic limit cycles can thus obtain a phase difference relative to the deterministic limit cycle, affecting the timekeeping precision. To compute this phase difference, we use the arclength change δs (see Fig. 4). δs is defined as the displacement $\mathbf{p}_j - \mathbf{p}_i$ projected onto the tangent unit vector $\hat{\mathbf{T}}$. The accumulated phase difference during one cycle is then $\delta\phi = 2\pi s/\ell$, with s the total arclength of one stochastic cycle (δs integrated over the full orbit) and ℓ the total arclength of the deterministic limit cycle. Phase diffusion increases with $\delta\phi$, in turn decreasing the timekeeping precision.

Figures 5(a) and 5(b) show the average accumulated phase difference $\langle \delta\phi \rangle$. For both laser amplitudes, $\langle \delta\phi \rangle$ first decreases and then increases with Δ_1/Γ. The rise in $\langle \delta\phi \rangle$ explains the drop in τ/σ_T at large Δ_1/Γ. However, in Fig. 5(b), the magnitude of the increase in $\langle \delta\phi \rangle$ at large Δ_1/Γ is much smaller than that of the drop in τ/σ_T observed in Fig. 3(b). This suggests that both the potential's curvature and phase diffusion influence the timekeeping precision. Indeed, Figs. 5(c) and 5(d) show that the ratio $\langle k/\delta\phi \rangle$ follows the same trends observed for τ/σ_T in Figs. 3(a) and 3(b). This reproduction of our experimental observations, for both laser powers, suggests that both tangent and normal fluctuations are relevant. In our system, the strength of both types of fluctuations depends on the laser-cavity detuning, which in turn determines the proximity of bifurcations. While our explanation is only qualitative, we highlight that we considered several other hypotheses to explain our results. However, none of these hypotheses yielded positive results. These hypotheses are related to the intracavity intensity in the limit-cycle regime, as well as the oscillation amplitude and phase space velocity of the limit cycle. A detailed discussion of those alternative (unsuccessful) hypotheses and accompanying analysis of our experimental data is presented in the Supplemental Material [44].

In summary, we explored the nontrivial relation between timekeeping precision and input power in the regime of strong fluctuations. By tuning the clock's operating point around different bifurcations, we demonstrated substantial timekeeping precision enhancements at constant input power and with minor frequency changes. The physics we elucidated is relevant to the design and energy-efficient operation of small timekeeping devices that must operate in the regime of strong fluctuations. To conclude, we offer two perspectives. One is to use our coupled-cavity system to test fundamental results in statistical physics, such as thermodynamic uncertainty relations constraining the precision of clocks [49]. This is an area with many theoretical results [1–9] but few experiments. Our work demonstrates the level of control required for experiments in that direction. These experiments could, in turn, reveal fundamental limits to the precision of clocks undergoing non-Markovian dynamics, as our system. The second

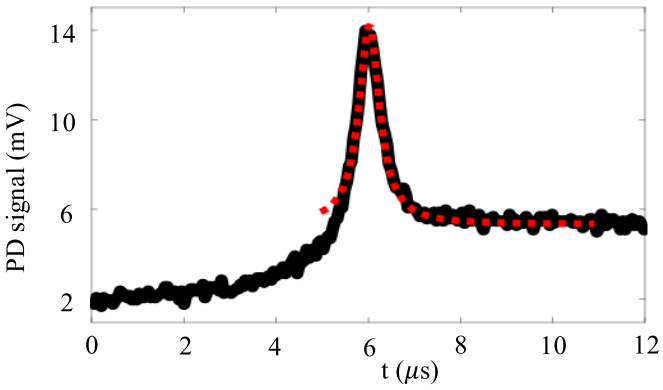

FIG. 6. Single-shot measurement of the transmitted intensity of the driven cavity (black) while the input laser is modulated by a chopper. Lorentzian fit to the overshoot is shown as a red dotted curve.

perspective we offer is related to the observation of limit cycles in the vicinity of a homoclinic bifurcation, as shown in Fig. 2(b). That regime is ideal for realizing the hallmark behavior of neurons, namely, excitability—the ability to release energy suddenly upon a small stimulus [17]. The realization of excitability in coupled-cavity systems would be a first step toward the realization of an all-optical spiking neural network.

This work is part of the research program of the Netherlands Organisation for Scientific Research (NWO). We thank Anne Spakman for preliminary measurements, Bart Verdonschot for discussions, and Aurélien Trichet for providing the structured mirror used in our experiments. S.R.K.R. acknowledges an ERC Starting Grant with Project No. 852694. B.B. and B.M. acknowledge support by FNRS-FRIA.

Data availability. The data that support the findings of this article are openly available [50].

Appendix A: Experimental system. The cavity mirrors are made of distributed Bragg reflectors (DBRs) on a glass substrate. The DBRs have 99.8% reflectance at 532 nm, the laser wavelength. The mirrors are aligned and positioned using piezoelectric actuators. One of the mirrors contains two partially overlapping concave features. These were milled with a focused ion beam on the glass substrate prior to the deposition of the DBR, as described in Ref. [51]. Each concave feature makes a plano-concave cavity. The cavity modes couple via their mutual field overlap [52,53]. This results in bonding and antibonding resonances, evident in the linear transmission spectrum in Fig. 1(b). The transmission through each concave mirror is measured by a separate avalanche photodetector. Details about our setup and measurement procedure are provided in the Supplemental Material [44].

Appendix B: Thermal relaxation time. We determined the thermal relaxation time τ of our oil-filled cavity system using the procedure introduced in Ref. [43]. The pump power is modulated in a steplike fashion using a chopper, while keeping the cavity length constant. Figure 6 shows in black a single-shot measurement of the transmitted intensity of the driven cavity as a function of time. Fitting a Lorentzian (red dotted curve) to the overshoot, we find a thermal relaxation time of $\tau = 1.2 \pm 0.1$ μs. This value is smaller than the 16 μs reported in Ref. [42] for a single-mode oil-filled cavity. We attribute this difference to a smaller mode volume for the experiments reported in this manuscript. The smaller mode volume is due to a tighter confinement in the transverse direction by concave mirrors with a smaller radius of curvature, as well as in the longitudinal direction by a shorter cavity length. A tighter confinement is indeed expected to reduce the thermal relaxation time [54].

Appendix C: Model. For our stochastic simulations and numerical parameter continuation, it is convenient to decompose $\alpha_j = u_j + iv_j$, with $u_j = \mathrm{Re}(\alpha_j)$ and $v_j = \mathrm{Im}(\alpha_j)$, and to define $w_j = U\int_0^t ds\, K(t-s)|\alpha_j(s)|^2$, such that Eq. (1) becomes

$$\begin{aligned}
\dot{u}_j &= -\left(\frac{\Gamma}{2} + \beta N_j\right)u_j - [\Delta_j - w_j]v_j - Jv_{3-j} + \sqrt{\kappa_L}[1-(-1)^j\rho]A + \frac{D}{\sqrt{2}}\xi_j', \\
\dot{v}_j &= -\left(\frac{\Gamma}{2} + \beta N_j\right)v_j + [\Delta_j - w_j]u_j + Ju_{3-j} + \sqrt{\kappa_L}[1-(-1)^j\rho]A + \frac{D}{\sqrt{2}}\xi_j'', \\
\dot{w}_j &= (UN_j - w_j)/\tau,
\end{aligned} \tag{C1}$$

with $N_j = |\alpha_j|^2 = u_j^2 + v_j^2$. Stochastic simulations are performed using a fourth-order Runge-Kutta algorithm with time increments of $\Gamma/10$ and a noise standard deviation of $D = \sqrt{\Gamma}/10$. Our simulations are performed with Gaussian white noise. The good agreement between experiments and simulations indicates that the experimental noise is approximately white within the relevant timescales. Steady-state solutions (obeying $\dot{u}_j = \dot{v}_j = \dot{w}_j = 0$) and bifurcation diagrams are obtained using numerical parameter continuation using MatCont [45].

The values of parameters in Eq. (C1) were determined as follows. First, note that Γ is fixed by the resonance linewidth at low pump power. The coupling strength J, intercavity detuning δ, and pump imbalance ρ are obtained by fitting the steady-state photon numbers $|\alpha_j|^2$ to the measurements in the linear regime [dashed curves in Fig. 1(b)]. From this, we obtain $J/\Gamma = 1$, $\delta/\Gamma = -0.25$, and $\rho = 0.95$. As explained in Ref. [42], the value of A only matters relative to the critical value for bistability, A_c, while κ_L only rescales the pump amplitude. By performing a series of measurements at increasing pump power, we determine the minimum power A_c^2 required for bistability, allowing us to reference all measurements to this value. The strength of the nonlinear dissipation $\beta = \Gamma/800$ is obtained by fitting the detuning range at which oscillations occur for $A = 3.9A_c$, keeping all other parameters fixed. The measured thermal relaxation time $\tau = 1.2$ μs is ∼6

orders of magnitude larger than Γ^{-1}, much too long to be able to simulate given computer memory and time restraints. In our calculations and simulations, we therefore take $\tau = 5000\Gamma^{-1}$, much longer than Γ^{-1}, but short enough that it can be simulated within reasonable time. We note, however, that it is shown in Ref. [17] that curves of Hopf bifurcations converge to a single curve for $\tau \gg \Gamma^{-1}$. We therefore expect no major differences if one were to use an even larger τ. The only free parameter left is U. However, the value of U only determines the minimum value of A for which bistability can be observed. Changing U does not qualitatively affect how the lineshape evolves with the laser amplitude A/A_c.

[1] A. C. Barato and U. Seifert, Thermodynamic uncertainty relation for biomolecular processes, Phys. Rev. Lett. **114**, 158101 (2015).

[2] A. C. Barato and U. Seifert, Cost and precision of Brownian clocks, Phys. Rev. X **6**, 041053 (2016).

[3] P. Erker, M. T. Mitchison, R. Silva, M. P. Woods, N. Brunner, and M. Huber, Autonomous quantum clocks: Does thermodynamics limit our ability to measure time? Phys. Rev. X **7**, 031022 (2017).

[4] M. Monti, D. K. Lubensky, and P. R. ten Wolde, Robustness of clocks to input noise, Phys. Rev. Lett. **121**, 078101 (2018).

[5] G. J. Milburn, The thermodynamics of clocks, Contemp. Phys. **61**, 69 (2020).

[6] A. N. Pearson, Y. Guryanova, P. Erker, E. A. Laird, G. A. D. Briggs, M. Huber, and N. Ares, Measuring the thermodynamic cost of timekeeping, Phys. Rev. X **11**, 021029 (2021).

[7] D. Ziemkiewicz, Entropy of timekeeping in a mechanical clock, Phys. Rev. E **105**, 055001 (2022).

[8] P. Pietzonka, Classical pendulum clocks break the thermodynamic uncertainty relation, Phys. Rev. Lett. **128**, 130606 (2022).

[9] A. Gopal, M. Esposito, and N. Freitas, Thermodynamic cost of precise timekeeping in an electronic underdamped clock, Phys. Rev. B **109**, 085421 (2024).

[10] S. H. Strogatz, *Nonlinear Dynamics and Chaos* (Perseus Books Publishing, Reading, MA, 1994).

[11] A. Jenkins, Self-oscillation, Phys. Rep. **525**, 167 (2013).

[12] J. del Pino, J. Košata, and O. Zilberberg, Limit cycles as stationary states of an extended harmonic balance ansatz, Phys. Rev. Res. **6**, 033180 (2024).

[13] C. Troein, J. C. Locke, M. S. Turner, and A. J. Millar, Weather and seasons together demand complex biological clocks, Curr. Biol. **19**, 1961 (2009).

[14] W. Pittayakanchit, Z. Lu, J. Chew, M. J. Rust, and A. Murugan, Biophysical clocks face a trade-off between internal and external noise resistance, eLife **7**, e37624 (2018).

[15] V. A. Makarov, V. I. Nekorkin, and M. G. Velarde, Spiking behavior in a noise-driven system combining oscillatory and excitatory properties, Phys. Rev. Lett. **86**, 3431 (2001).

[16] V. Buendía, S. di Santo, P. Villegas, R. Burioni, and M. A. Muñoz, Self-organized bistability and its possible relevance for brain dynamics, Phys. Rev. Res. **2**, 013318 (2020).

[17] B. Braeckeveldt, K. J. H. Peters, B. Verdonschot, B. Maes, and S. R. K. Rodriguez, Memory-induced excitability in optical cavities, Phys. Rev. Res. **6**, 023008 (2024).

[18] L. A. Orozco, A. T. Rosenberger, and H. J. Kimble, Intrinsic dynamical instability in optical bistability with two-level atoms, Phys. Rev. Lett. **53**, 2547 (1984).

[19] M. Marconi, F. Raineri, A. Levenson, A. M. Yacomotti, J. Javaloyes, S. H. Pan, A. El Amili, and Y. Fainman, Mesoscopic limit cycles in coupled nanolasers, Phys. Rev. Lett. **124**, 213602 (2020).

[20] S. Kim, Y. G. Rubo, Timothy C. H. Liew, S. Brodbeck, C. Schneider, S. Höfling, and H. Deng, Emergence of microfrequency comb via limit cycles in dissipatively coupled condensates, Phys. Rev. B **101**, 085302 (2020).

[21] N. C. Zambon, S. R. K. Rodriguez, A. Lemaître, A. Harouri, L. Le Gratiet, I. Sagnes, P. St-Jean, S. Ravets, A. Amo, and J. Bloch, Parametric instability in coupled nonlinear microcavities, Phys. Rev. A **102**, 023526 (2020).

[22] J. Abad-Arredondo, Z. Geng, G. Keijsers, F. Bijloo, F. J. García-Vidal, A. I. Fernández-Domínguez, and S. R. K. Rodriguez, Spontaneous symmetry breaking in diffraction, Phys. Rev. Lett. **133**, 133803 (2024).

[23] K. J. H. Peters and S. R. K. Rodriguez, Limit cycles and chaos induced by a nonlinearity with memory, Eur. Phys. J. Spec. Top. **231**, 247 (2022).

[24] E. Zheng, M. Brandenbourger, L. Robinet, P. Schall, E. Lerner, and C. Coulais, Self-oscillation and synchronization transitions in elastoactive structures, Phys. Rev. Lett. **130**, 178202 (2023).

[25] C. Metzger, M. Ludwig, C. Neuenhahn, A. Ortlieb, I. Favero, K. Karrai, and F. Marquardt, Self-induced oscillations in an optomechanical system driven by bolometric backaction, Phys. Rev. Lett. **101**, 133903 (2008).

[26] M. Bagheri, M. Poot, L. Fan, F. Marquardt, and H. X. Tang, Photonic cavity synchronization of nanomechanical oscillators, Phys. Rev. Lett. **111**, 213902 (2013).

[27] P. Piergentili, W. Li, R. Natali, D. Vitali, and G. Di Giuseppe, Absolute determination of the single-photon optomechanical coupling rate via a Hopf bifurcation, Phys. Rev. Appl. **15**, 034012 (2021).

[28] V. Liška, T. Zemánková, P. Jákl, M. Šiler, S. H. Simpson, P. Zemánek, and O. Brzobohatý, *PT*-like phase transition and limit cycle oscillations in non-reciprocally coupled optomechanical oscillators levitated in vacuum, Nat. Phys. **20** 1622 (2024).

[29] L. G. Villanueva, E. Kenig, R. B. Karabalin, M. H. Matheny, R. Lifshitz, M. C. Cross, and M. L. Roukes, Surpassing fundamental limits of oscillators using nonlinear resonators, Phys. Rev. Lett. **110**, 177208 (2013).

[30] A. Shapere and F. Wilczek, Classical time crystals, Phys. Rev. Lett. **109**, 160402 (2012).

[31] J. Zhang, P. W. Hess, A. Kyprianidis, P. Becker, A. Lee, J. Smith, G. Pagano, I.-D. Potirniche, A. C. Potter, A. Vishwanath, *et al.*, Observation of a discrete time crystal, Nature (London) **543**, 217 (2017).

[32] J. Smits, L. Liao, H. T. C. Stoof, and P. van der Straten, Observation of a space-time crystal in a superfluid quantum gas, Phys. Rev. Lett. **121**, 185301 (2018).

[33] T. L. Heugel, M. Oscity, A. Eichler, O. Zilberberg, and R. Chitra, Classical many-body time crystals, Phys. Rev. Lett. **123**, 124301 (2019).

[34] J. Randall, C. E. Bradley, F. V. van der Gronden, A. Galicia, M. H. Abobeih, M. Markham, D. J. Twitchen, F. Machado, N. Y.

Yao, and T. H. Taminiau, Many-body–localized discrete time crystal with a programmable spin-based quantum simulator, Science **374**, 1474 (2021).

[35] H. Keßler, P. Kongkhambut, C. Georges, L. Mathey, J. G. Cosme, and A. Hemmerich, Observation of a dissipative time crystal, Phys. Rev. Lett. **127**, 043602 (2021).

[36] L. Oberreiter, U. Seifert, and A. C. Barato, Stochastic discrete time crystals: Entropy production and subharmonic synchronization, Phys. Rev. Lett. **126**, 020603 (2021).

[37] P. Kongkhambut, J. Skulte, L. Mathey, J. G. Cosme, A. Hemmerich, and H. Keßler, Observation of a continuous time crystal, Science **377**, 670 (2022).

[38] M. P. Zaletel, M. Lukin, C. Monroe, C. Nayak, F. Wilczek, and N. Y. Yao, Colloquium: Quantum and classical discrete time crystals, Rev. Mod. Phys. **95**, 031001 (2023).

[39] I. Carraro-Haddad, D. L. Chafatinos, A. S. Kuznetsov, I. A. Papuccio-Fernández, A. A. Reynoso, A. Bruchhausen, K. Biermann, P. V. Santos, G. Usaj, and A. Fainstein, Solid-state continuous time crystal in a polariton condensate with a built-in mechanical clock, Science **384**, 995 (2024).

[40] R. Daviet, C. P. Zelle, A. Asadollahi, and S. Diehl, Kardar-Parisi-Zhang scaling in time-crystalline matter, Phys. Rev. Lett. **135**, 047101 (2025).

[41] T. L. Heugel, A. Eichler, R. Chitra, and O. Zilberberg, The role of fluctuations in quantum and classical time crystals, SciPost Phys. Core **6**, 053 (2023).

[42] Z. Geng, K. J. H. Peters, A. A. P. Trichet, K. Malmir, R. Kolkowski, J. M. Smith, and S. R. K. Rodriguez, Universal scaling in the dynamic hysteresis, and non-Markovian dynamics, of a tunable optical cavity, Phys. Rev. Lett. **124**, 153603 (2020).

[43] K. J. H. Peters, Z. Geng, K. Malmir, J. M. Smith, and S. R. K. Rodriguez, Extremely broadband stochastic resonance of light and enhanced energy harvesting enabled by memory effects in the nonlinear response, Phys. Rev. Lett. **126**, 213901 (2021).

[44] See Supplemental Material at http://link.aps.org/supplemental/10.1103/pym4-3csj for details about the experimental setup, validation of our model across a wide parameter range, experimental signatures of predicted bifurcations, changes in limit-cycle amplitude with detuning, and the precision in relation to intracavity intensity, oscillation amplitude, and phase space velocity.

[45] A. Dhooge, W. Govaerts, and Y. A. Kuznetsov, MATCONT: A MATLAB package for numerical bifurcation analysis of ODEs, ACM Trans. Math. Softw. **29**, 141 (2003).

[46] M. Dykman and M. Krivoglaz, Fluctuations in nonlinear systems near bifurcations corresponding to the appearance of new stable states, Physica A **104**, 480 (1980).

[47] E. Knobloch and K. Wiesenfeld, Bifurcations in fluctuating systems: The center-manifold approach, J. Stat. Phys. **33**, 611 (1983).

[48] C. Meunier and A. Verga, Noise and bifurcations, J. Stat. Phys. **50**, 345 (1988).

[49] R. Marsland, III, W. Cui, and J. M. Horowitz, The thermodynamic uncertainty relation in biochemical oscillations, J. R. Soc. Interface **16**, 20190098 (2019).

[50] https://zenodo.org/records/17963773.

[51] A. A. P. Trichet, P. R. Dolan, D. M. Coles, G. M. Hughes, and J. M. Smith, Topographic control of open-access microcavities at the nanometer scale, Opt. Express **23**, 17205 (2015).

[52] S. Dufferwiel, F. Li, A. Trichet, L. Giriunas, P. Walker, I. Farrer, D. Ritchie, J. Smith, M. Skolnick, and D. Krizhanovskii, Tunable polaritonic molecules in an open microcavity system, Appl. Phys. Lett. **107**, 201106 (2015).

[53] L. Flatten, A. Trichet, and J. Smith, Spectral engineering of coupled open-access microcavities, Laser Photonics Rev. **10**, 257 (2016).

[54] E. Stein, F. Vewinger, and A. Pelster, Collective modes of a photon Bose-Einstein condensate with thermo-optic interaction, New J. Phys. **21**, 103044 (2019).